PHYSICAL REVIEW B **77**, 064301 (2008)

Atomic form-factor measurements in the low-momentum transfer region for Li, Be, and Al by inelastic x-ray scattering

A. Alatas,[1,*] A. H. Said,[1,2] H. Sinn,[1] G. Bortel,[1,†] M. Y. Hu,[1,‡] J. Zhao,[1] C. A. Burns,[2] E. Burkel,[3] and E. E. Alp[1]
[1]*Argonne National Laboratory, Argonne, Illinois 60439, USA*
[2]*Western Michigan University, Kalamazoo, Michigan 49008, USA*
[3]*University of Rostock, 18055 Rostock, Germany*

(Received 31 August 2007; revised manuscript received 13 December 2007; published 1 February 2008)

We report measurements of the atomic form factor of lithium, beryllium, and aluminum single crystals at low-momentum transfers ($Q=1.6-50\ \mathrm{nm}^{-1}$) from the intensity of phonons observed by inelastic x-ray scattering. Comparing to Hartree-Fock calculations, the form factor deviates significantly in the case of lithium and beryllium around k_F. These deviations can be mostly understood on the basis of electron redistribution by a pseudopotential. The influence of multiple scattering due to coherent phonon scattering and possible deviations from the adiabatic approximation are also discussed.

DOI: 10.1103/PhysRevB.77.064301 PACS number(s): 63.20.D−, 63.20.K−, 78.70.Ck

I. INTRODUCTION

X-ray atomic form factors for free atoms and ions are required in numerous crystallographic calculations, in particular, least-squares structure refinement. The atomic form factor is described as a Fourier transform of the electron distribution and carries information on the electron wave function. Tabulated values for free atoms and ions obtained from atomic wave functions can be found in literature.[1] However, atomic form factors in bonded environments are different from those of isolated atoms due to the reconfiguration of the valence electron distribution.

Generally speaking, the bonds that bind a solid can be classified as one of four types: van der Waals, ionic, covalent, and metallic. The fundamental question about the mechanism of bonding is related to the alterations of the electronic states of the individual atoms when they form the solid. Both the ionic case, with the complete transfer of an electron, and the weak interaction of the van der Waals force make treatments of these systems fairly straightforward. However, the changes due to covalent and metallic bondings are more subtle. In metals, the binding is mainly due to the anisotropic redistribution of the valence electrons that become the conduction electrons. These conduction electrons are spread out over several atomic spacings. Since the lowest order Bragg reflections from x-ray measurements correspond to changes in the electronic distribution on length scales of order of the atomic spacing, these data from the lowest order Bragg reflections are only of limited use. Even for most cases, these data are usually not considered in the structure refinement procedure to avoid the bonding effect.[2]

On the other hand, over the last 30 years, the two-component nature of liquid metals has been widely accepted and scattering cross sections have been expressed in terms of separate ion-ion, ion-electron, and electron-electron correlation functions in theoretical and experimental studies. In this approach, the conduction electron distribution in the small-momentum transfer region becomes an important part in the determination of the ion-electron structure factor $S_{ie}(Q)$, since $S_{ie}(Q)$ is represented in terms of the ion-ion structure factor $S_{ii}(Q)$ and the charge distribution around a pseudoatom, $\rho_{el}(Q)$.[3–5]

Much of the work related to electron-ion correlation is concentrated around liquid metals, since they are well known to be binary mixture of ions and conduction electrons.[4] In these studies, however, the structure factor of a liquid metal measured by the x-ray method is extracted from the free-atom form factor by assuming that a liquid metal can be taken as an assembly of isolated atoms. The main motivation of this paper is to show experimentally that the bonding leads to a redistribution of valence electrons and how that alters x-ray intensities in the small-Q region.

As pointed out by Chihara[3] and others,[4] changes in the valence electron density distribution affect the coherent part of the x-ray scattering cross section by a modification of the x-ray form factor $f(Q)$:

$$f(Q)=\rho_{el}(Q)+f_{ion}(Q), \tag{1}$$

where $\rho_{el}(Q)$ is the effective screening density in Fourier space (the form factor of the pseudoatom), which represents the average density of conduction electrons that surrounds each ion relative to the uniform background, and $f_{ion}(Q)$ is the atomic form factor of the core electrons. It is this difference in $\rho_{el}(Q)$ from free-atom form factors that indicates a measure of the change in electron density upon bonding. This effect becomes more visible when the ratio of the number of valence electrons Z to the total number of electrons, Z_A, increases in the system. The changes in the form factors associated with the effect of the bonding for several liquid metals were recently calculated within the quantum hypernetted chain (QHNC) approximation,[5] which self-consistently combines integral equation techniques from the theory of liquids with a Kohn-Sham-type treatment of electrons.

Several studies on the static structure factor of simple liquids comparing x-ray scattering and neutron scattering results have been conducted.[6–8] However, because a number of difficult corrections such as multiphonon scattering, self-absorption, and incoherent scattering have to be performed on both data sets, the results are sometimes ambiguous. For example, the incoherent x-ray scattering in the case of liquid metals—the so-called Compton correction—turns out to be substantially different for the light elements than the usually tabulated Hartree-Fock calculations.[6,9] In the case of neutron scattering, on the other hand, a measurement of the static structure factor is, in general, complicated by the presence of an incoherent cross section and, for high-sound-velocity liquids, possibly incomplete due to the fact that the Brillouin modes in the dynamic structure factor at low Q are experimentally difficult to reach and, therefore, the so-called Placzek correction fails.[10]

A new opportunity to shed light on this problem is made possible by method of inelastic x-ray scattering.[11,12] Because of the high resolving power in energy of 10^{-8}, the incoherent part of the cross section (Compton scattering) has no effect on the phonon spectra. In contrast to several previous x-ray studies of Bragg intensities,[13–16] x-ray form factors can now be obtained from phonon intensity measurements; therefore, the accessible Q range in this case is not limited to the occurrence of Bragg reflections. Because of this, deviations of the valence electron form factor can be directly measured in the low-Q range, where the largest differences compared to the Hartree-Fock distribution are expected.

The observed x-ray intensity from phonons is described by the partial differential cross section as

$$\frac{d^2\sigma}{d\Omega d\omega} = N\left(\frac{d\sigma}{d\Omega}\right)_{Th} S(\mathbf{Q},\omega), \tag{2}$$

where the first term is the Thomson scattering cross section, and the second term is the dynamical structure factor, which depends on the properties of the sample. The dynamical structure factor for the one-phonon case is given as[17]

$$S(\mathbf{Q},\omega) = \sum_{\mathbf{q},j}\left|\sum_{s}^{unit\ cell} f_s(Q)\frac{\hbar}{\sqrt{2m_s}}e^{-W_s(Q)}e^{i\mathbf{Q}\cdot\mathbf{R}_s}[\mathbf{Q}\cdot\mathbf{e}(\mathbf{q},s,j)]\right|^2 \times \frac{\left\langle n_j+\frac{1}{2}\pm\frac{1}{2}\right\rangle}{\omega_{\mathbf{q}j}}\delta(\omega\mp\omega_{\mathbf{q}j}), \tag{3}$$

where j is the index of the phonon branch, m_s is the mass of atom s, n_j is the population number, $e^{-W_s(Q)}$ is the Debye-Waller factor, and $\mathbf{e}(\mathbf{q},s,j)$ is the eigenvector of the phonon. The upper and lower signs refer to phonon creation (i.e., photon energy loss) and annihilation (i.e., photon energy gain) parts, and s is the index of the atoms within the unit cell. Lithium and aluminum have one atom per unit cell. For this reason, sum in this equation does not apply for both of them. The case is similar for beryllium despite the two atoms per unit cell, since it has a nonsymmorphic space group.

Here, we report measurements of the relative intensities of phonons in high-quality single crystals of lithium, beryllium, and aluminum using inelastic scattering in the low-Q region. They are all considered to be simple metals. The main advantage of using single crystals over liquids for form-factor measurements is the reduction of both strong elastic scattering and multiphonon scattering. Therefore, the intensities can be predicted accurately once the phonon dispersion curves are known.

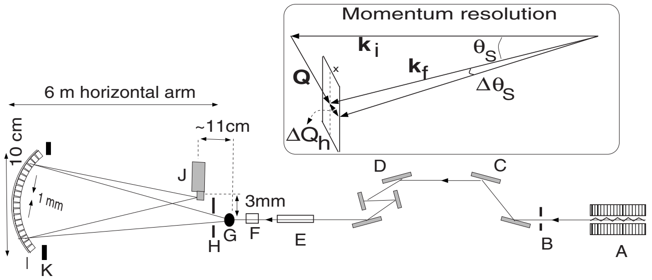

FIG. 1. Schematic view of the spectrometer developed at beamline 3-ID. The beam comes from an undulator (A) and premonochromator (C) and then passes through the high-resolution monochromator (D) and focusing mirror (E) before it illuminates the sample (G). The scattered intensity is focused by an analyzer (I) into the detector (J). The ionization chamber (F) is used to monitor the incident flux on the sample. The slit systems that determine the source size are (B) and (H). The momentum resolution is determined by a slit (K) in front of the analyzer that has a slit opening of x in the real space. In the reciprocal space, half width of the momentum resolution is represented by ΔQ_h. The momentum-transfer vector and the incident beam wave vector are represented by $\mathbf{Q}$ and $\mathbf{k}_i$, respectively. The scattering angle is represented by θ_s and the deviation of the scattering angle is shown by $\Delta\theta_s$.

II. EXPERIMENT

These experiments were performed at the Advanced Photon Source beamline 3-ID with an incident x-ray energy of 21.657 keV and the general setup is shown in Fig. 1.

The spectrometer is working in horizontal scattering geometry with a horizontally polarized radiation. The requirements for very high energy resolution and the basic principles of such instrumentation are discussed elsewhere.[18–21] The size of the beam focused on the sample is $0.25\times0.25\ \text{mm}^2$. The energy-resolution function of the spectrometer is experimentally determined from a Plexiglas sample. The resolution function was parametrized by a pseudo-Voigt function with a mixing parameter of 0.59 of Lorentzian and Gaussian curves with a total full width at half maximum of 2.1 meV. The resolution is constant over the measured momentum transfer range within the experimental error of ±0.1 meV.

In the study of collective excitations, the availability of the flux from the x-ray source is the most important limitation. Therefore, one tries to collect the inelastic signal in a large solid angle as possible. On the other hand, this will introduce an uncertainty in the momentum space, affecting the exact energy position of the phonon excitation especially around the zone center where the slope of the dispersion curve may become very steep. The desired momentum resolution can be defined by a slit system in front of the analyzer. This situation is also shown in the inset of Fig. 1 for a scattering geometry represented in momentum space. The difference in momentum transfer points at $\theta_S+\Delta\theta_S$ and θ_S determines the half width of the horizontal momentum resolution, ΔQ_h, and can be written as

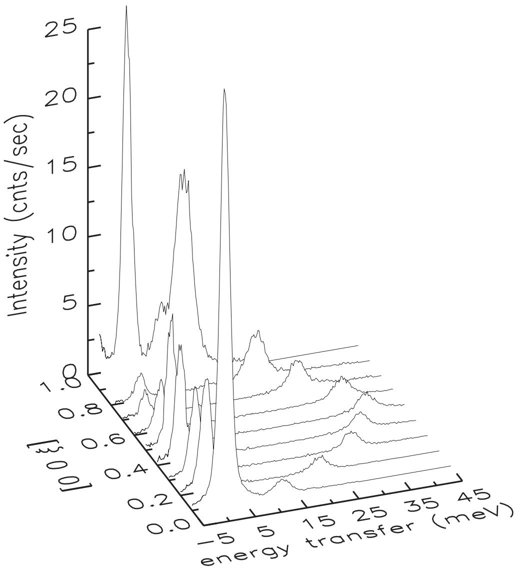

FIG. 2. Energy scans for lithium along the $[0\ \zeta\ \zeta]$ direction for longitudinal modes.

$$\Delta Q_h = Q_{\theta_S+\Delta\theta_S} - Q_{\theta_S} = 2k_i\left[\sin\left(\frac{\theta_S+\Delta\theta_S}{2}\right) - \sin\left(\frac{\theta_S}{2}\right)\right], \tag{4}$$

where $\Delta\theta_S = \arcsin\left(\frac{x}{2L}\right)$ is in real space. In our experiment, we used two different momentum resolutions at the horizontal direction, ± 0.36 and $\pm 0.18\ \mathrm{nm}^{-1}$, which correspond to horizontal slit sizes of 4 and 2 cm, respectively. The momentum resolution in this direction stays constant within 1% for all scattering angles accessible with our instrument. The size of the vertical slits was chosen such that the influence on the momentum resolution was negligible.

A 10-mm-diameter cylindrical and 99.8%-pure lithium, a 13-mm-diameter cylindrical and 99.999%-pure beryllium, and a 2.05-mm-thick (rectangular) and 99.9999%-pure aluminum single crystals were used in an evacuated sample container. Absorptions at 21.657 keV are 10% for lithium, 40% for beryllium, and 78% for aluminum. These materials are representative of monovalent, divalent, and trivalent metals, and they are in the order of increasing electronic density. The rocking curves for beryllium and aluminum (0 0 2) reflections and for lithium (0 1 1) reflection show that the peak widths are about 0.02°, 0.05°, and 0.03°, respectively.

Figures 2–4 show the spectra corresponding to measurements at different momentum transfers along the $[0\ \zeta\ \zeta]$ direction for lithium and along the $[0\ 0\ \zeta]$ direction for beryllium and aluminum, respectively. The energy scans are done by changing the incident energy by rotating the in-line multi-Bragg diffracting high-resolution monochromator crystals,[18] while the energies of the excitations are selected by the fixed energy of the analyzer.[22] In these measurements, phonon intensities are normalized to incoming flux on the sample monitored by the ionization chamber detector. The total flux on the sample was 3×10^8 photons/s/meV. At each Q point, an optimization of the analyzer alignment was performed with a Plexiglas reference sample. Due to the presence of the elastic scattering, only the energy-loss side of the excitations was recorded in the case of lithium and beryllium (Figs. 2 and 3). Excitation energies of beryllium were determined from the difference of zero-energy point (i.e., elastic peak) and the phonon peak. In principle, one should not observe any elastic line in the case of single crystals away from the Bragg peak, but impurities inside the crystal act as scattering points and contribute as a background around the elastic line. Most of this effect is minimized by a factor of 2 using

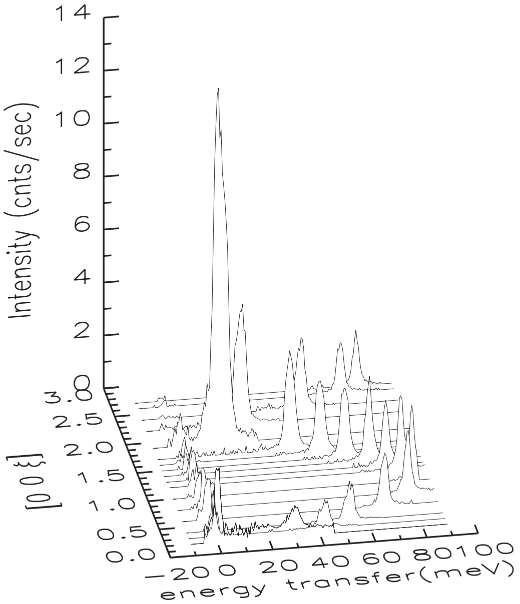

FIG. 3. Energy scans for beryllium along the $[0\ 0\ \zeta]$ direction for longitudinal modes.

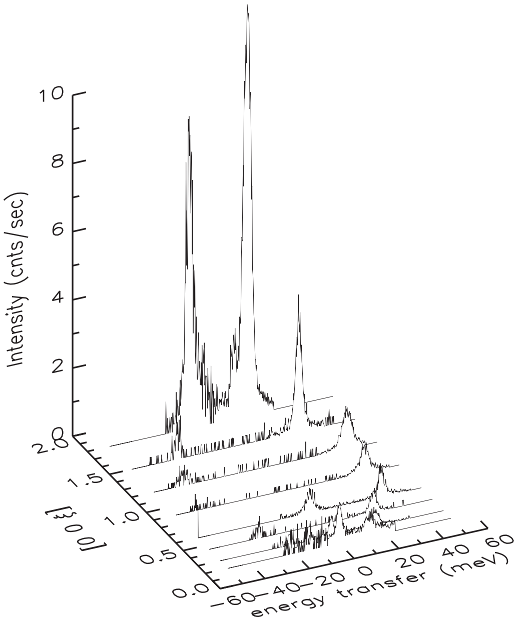

FIG. 4. Energy scans for aluminum along the $[0\ 0\ \zeta]$ direction for longitudinal modes. The elastic scattering at $\zeta=0.6$ is due to air scattering.

99.999%-pure high-quality single-crystal beryllium instead of 99.98%-pure crystal, yet elastic peak intensities are observed for beryllium as we go to higher momentum transfer points with decreasing intensities. A similar kind of elastic scattering was also observed for lithium (Fig. 2), but most of the elastic scattering was due to oil on the surface of the lithium in this case. On the other hand, elastic peaks were not observed for aluminum. When elastic scattering intensities of beryllium are compared to Hartree-Fock calculation of the valence electron form factor ($f_{atom}-f_{ion}$) as a function of momentum transfer (Q), they show the same Q dependence, i.e., they go down to zero as they approach the first Bragg peak position. This may be interpreted as at any instant a small fraction of the valence electrons in beryllium scatters elastically, i.e., the deviation from the adiabatic approximation may be present for a small fraction of the valence electrons in beryllium.[21] In the case of aluminum, both the energy-loss and energy-gain sides of the excitations were recorded to determine the energy scale for aluminum except for the $\zeta=0.6$ scan. Measurements were carried out for momentum transfers up to $\zeta=3$, but spectra in Fig. 4 are shown only up to $\zeta=1.8$.

As we attempt to achieve a relative energy resolution of the order of 10^{-8}, the stability of the crystal temperature becomes an important issue. Very high energy resolution requires temperature stability of the order of millikelvins. With an enclosure around the monochromator, temperature stability of 120 mK/12 h was achieved for the high-resolution monochromator. The temperature of the analyzer was controlled with a stability of 20 mK/12 h with the enclosure and the water-cooled base plate. Temperatures of the crystals were recorded by calibrated thermistors at all times during the experiment, and temperature corrections are applied by software.

III. DATA ANAYLSIS

The inelastic x-ray scattering (IXS) spectra were analyzed by two model functions: damped harmonic oscillator (DHO) model function[23] convoluted with the resolution function and pseudo-Voigt model function. They were used to extract the values of the following parameters: integrated intensity, energy position of the excitation, and width. Some of the fits are shown in Fig. 5(a) for different momentum transfer points in terms of the reduced wave units.

The phonon dispersion relations determined from the energy positions of the measured data are presented in Fig. 6 for the longitudinal modes of lithium, beryllium, and aluminum together with their widths. Phonon widths deconvoluted from the energy resolution are shown in this figure. Dispersion relations are in excellent agreement with results from inelastic neutron scattering.[24–26] Since the measurements are performed with a certain momentum resolution of the analyzer as mentioned before, distribution of this momentum resolution introduces a distribution in the excitation energy, i.e., the measured phonon width is affected by this energy distribution. Therefore, a precise phonon width calculation requires deconvolution of that energy distribution from the measured width in addition to deconvolution of the energy resolution of the spectrometer. Even though precise determination of the phonon width is not in the scope of this paper, we will briefly talk about the phonon widths for the sake of completeness of the paper. Since the dispersion relation of phonon excitations can be approximated by a sine function,

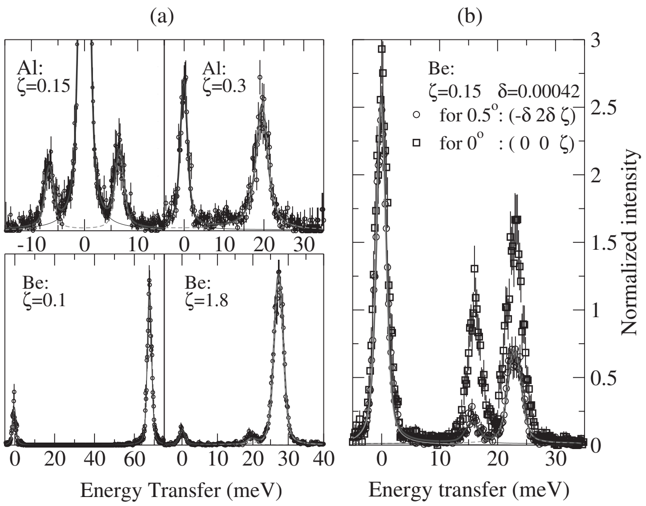

FIG. 5. (a) Some of the energy scans for different momentum positions in terms of the reduced wave unit ζ are shown with circles, and fits to these data are shown with thick gray lines. (b) Energy scans for beryllium at $\zeta=0.15$ ($Q=2.63$ cm^{-1}) for two different tilt angle positions rotated around incident x-ray direction showing an increase in the intensity due to coherent phonon scattering caused by the additional wave field inside the crystal induced by the (0 1 3) Bragg reflection.

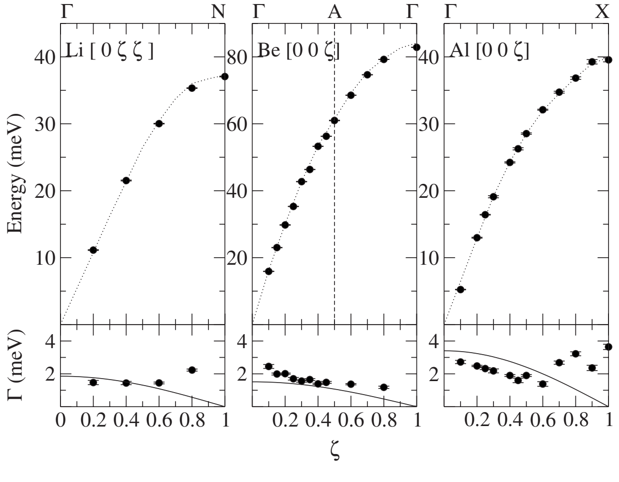

FIG. 6. Dispersion relations for lithium along the [0 ζ ζ] direction, and for beryllium and aluminum along the [0 0 ζ] direction. Circles are present measurements. Dotted lines are results from inelastic neutron scattering experiments (Refs. 24–26). The lower pictures are the full width of half maximum of the phonon peaks deconvoluted from the spectrometer's overall energy resolution. Thus, Γ projects to zero at the zone boundary where there should be no contribution from dispersion. Solid lines are the theoretical calculations of the widths due to finite momentum resolution that contributes to measured width. It is calculated from sine function of a dispersion relation (Ref. 27) as explained in the text.

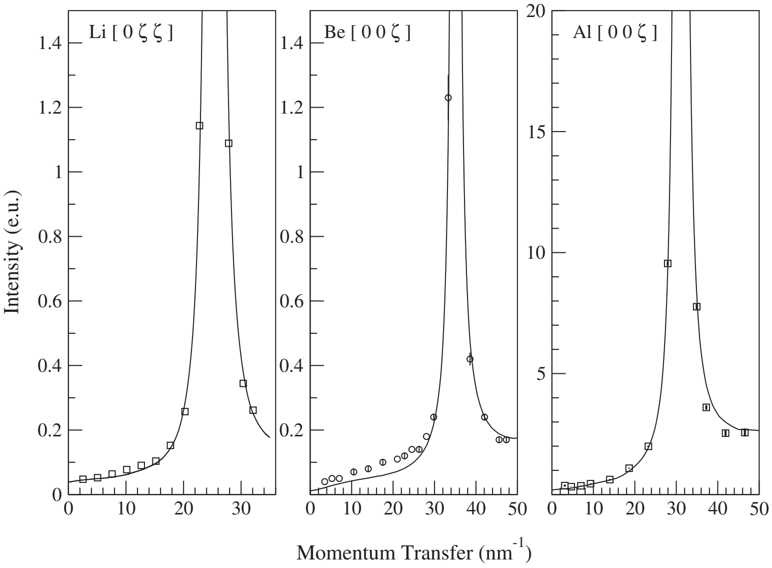

FIG. 7. Adjusted measured integrated intensities for lithium, beryllium, and aluminum. The conversion of integrated intensity to electron units include as adjustable parameter the analyzer efficiency, the accuracy of which is estimated to be around 20%, as explained in the text. Circles represent the data from the pseudo-Voigt model for beryllium, and squares represent the data from the DHO model for lithium and aluminum. Solid lines are the theoretical calculations.

the energy distribution due to momentum resolution can be calculated from this relation.[21,27] In Fig. 6, the energy widths calculated from this sine function are compared to measured phonon widths. In the case of lithium, they show different behavior around the zone boundary. Even though the calculation goes to a minimum at the zone boundary, measured widths show some extra broadening at the zone boundary. This is also reported in the neutron experiment[24] and explained as an effect of anharmonicity. The same effect is also observed around the zone boundary for aluminum. This is also in agreement with neutron measurement.[25] The broadening around the zone boundary in this case was interpreted as due to phonon-phonon interaction. In the case of beryllium, theoretical and measured widths closely follow each other indicating that intrinsic widths of phonons do not change with the momentum transfer and are much smaller than the instrumental resolution.

From the fitting routine, the measured integrated intensities of the phonon creation parts are derived. Then, measured intensities are corrected for several factors in order to get absolute intensity in electron units, which is derived from Eq. (2). It is described as

$$I^{e.u.} = \frac{\dfrac{I}{I_0}}{\delta\theta\delta\alpha r_0^2 P^2(\theta_s) K_{abs}(\rho,\tau,\theta_s) V_s(Q)\,\eta_{eff} e^{-2W}}, \qquad (5)$$

where $\delta\theta$ and $\delta\alpha$ are the horizontal and vertical sizes of the analyzer slits. The classical electron radius is r_0. The polarization factor is defined as $P^2(\theta_s)$. The Debye-Waller factor is e^{-2W}. The term related to the absorption of the beam in the sample is $K_{abs}(\rho,\tau,\theta_s)$. As the sample is rotated to different momentum transfer points, the volume of the sample, $V_s(Q)$, involved in the scattering process changes. The scattering volume for different scattering angles was calculated with a FORTRAN program for the given sample geometry. The effective scattering volume of samples for lithium and beryllium are reduced by 50%–60% at their highest scattering angle and for aluminum, it was about 5%.

The measured integrated intensities, corrected for the several factors as discussed above, are then compared to theoretical structure factor for the phonon creation part, $S_C(Q)$. It is derived from Eq. (3) and can be written as

$$S_C(Q) \propto \frac{f^2(Q)Q^2}{m\omega}\langle n(\omega)+1\rangle. \qquad (6)$$

A χ^2 minimization method is used in this comparison. The reason for this is that direct measurement of the analyzer efficiency η_{eff} is not precise enough with a reference sample like Plexiglas. For this reason, scale factor is introduced in χ^2 minimization to take account of the efficiency of the analyzer. Also, previous atomic form-factor measurements determined from Bragg reflections[13,16] are used as a constrain at the high Q limit of our measurements. From this procedure, the phonon measurements described here were used to determine analyzer efficiency of around 20% by leaving it as the only unknown (scaling factor) in Eq. (5). Adjusted measured integrated intensities of the lithium and beryllium and aluminum are reported in Fig. 7 with theoretical calculation of $S_C(Q)$ (solid line) using a tabulated Hartree-Fock form factor for a free atom. In the beryllium case as given in Fig. 7, a systematic deviation from theory curve is observed in the low-momentum region $0<Q(\mathrm{nm}^{-1})<25$. This indicates that the electron distribution may change upon bonding from the free-atom form factor. On the other hand, comparison of measured and theoretical calculations for aluminum shows better overall agreement in Fig. 7.

A rather important correction in the data was the occurrence of multiple scattering (coherent phonon scattering). This effect has been used, e.g., in an experiment to determine phases of phonons.[28] Similar interference effects have also been exploited in experiments to observe coherent Compton scattering.[29] Recently, coherent phonon scattering is reported for silicon.[30] Multiple scattering as analog to multiple Bragg excitations occurs when, at a particular momentum transfer $(m\ n\ o)$, a Bragg reflection $(h\ k\ l)$ is simultaneously excited. These reflected photons travel inside the sample and are scattered a second time inelastically by $(m-h\ n-k\ o-l)$ giving additional phonon scattering from a higher Brillouin zone (BZ) that can add coherently.

An example is shown in Fig. 5(b) for the beryllium crystal. The (0 1 3) Bragg reflection is simultaneosly excited when the crystal is oriented for the (0 0 0.15) momentum transfer point. For this specific orientation, the phonon intensity was doubled due to the presence of the second phonon scattering process at (0 −1 −2.85). In addition, the transverse phonon was strongly visible at this point, although it is not allowed in the first BZ along the $[0\ 0\ \zeta]$ direction since the eigenvector of the transverse mode is perpendicular to the momentum transfer vector **Q**. A similar situation was also observed for lithium, but it was not as strong as in the beryllium case. We observed this type of multiple scattering by monitoring Bragg reflections with a fluorescence screen. When the crystal is tilted about 0.5°, we moved into new point $(-\delta\ 2\delta\ 0.15)$ in the reciprocal space where $\delta = 0.000\,42$, and the multiple scattering could be suppressed [Fig. 5(b)]. For this new point, the eigenvector is calculated from the package program UNISOFT,[31] and the effect on the intensity is less than 1% within the error bar when it is compared to the (0 0 0.15) point. The origin of the intensity at the position of the transverse phonon in the $(-\delta\ 2\delta\ 0.15)$ point is due to vertical momentum resolution of the analyzer. Multiphonon scattering that involves a two-phonon scattering process,[32] which is different than this interference effect, was assumed to cause the rather broad background and is negligible at small-Q values.

IV. RESULTS AND DISCUSSION

Atomic form factors were extracted from the adjusted measured integrated intensities of the phonon excitations. They are shown in Fig. 8 with circles and compared to Hartree-Fock calculations of the free-atom form factor (solid line) using the χ^2 minimization method. In addition, the measured form factor is also compared to QHNC calculation of Anta and Louis[5] with dashed lines at the left side in Fig. 8, showing a much better agreement with the experimental data. χ^2 values are as follows: 3.34–2.68 for lithium, 5.50–2.04 for beryllium, and 6.31–2.62 for aluminum. Here, the first number is for Hartree-Fock calculation and the second number is for the QHNC calculation of Anta and Louis. The experimental data for lithium and beryllium show a less rapidly decaying form factor for the ions in the metal than for the free atom, suggesting that the valence electrons must be more concentrated on the ion than on the atom. The deviations of the measured form factor from the free-atomic form factor, Δ, in terms of a fraction of the valence electron are plotted on the right side of Fig. 8 together with the deviations of the theoretical calculation (dashed line). For lithium and beryllium, 20% of the valence electrons is excess charge around k_F and extended over about $1.7k_F$ (where k_F is defined as Fermi wave vector). In the case of aluminum, the measured experimental data are in agreement with both form-factor calculations for the region $Q > 14\ \text{nm}^{-1}$ $(0.8k_F)$, whereas for $Q \leq 14\ \text{nm}^{-1}$, our measurements fluctuate strongly. This can be understood from the relatively smaller weight of the x-ray scattering intensities from the valence electrons in aluminum as compared to lithium and beryllium.

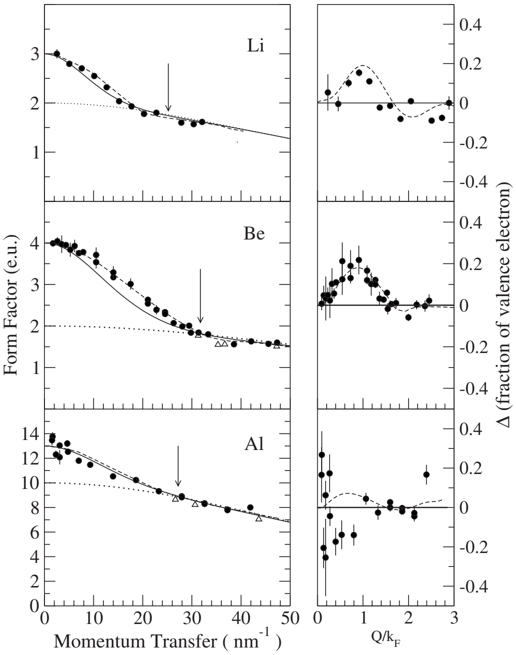

FIG. 8. Comparison of measured atomic form factor (circles) with the free-atom Hartree-Fock calculation (solid line) and the metallic-atom form factor calculated by the QHNC approximation (dashed line) for a given direction of lithium, beryllium and aluminum. The dotted line is the ionic form factor from Hartree-Fock calculation. Triangles show the experimental data determined from Bragg reflections (Refs. 13 and 16). The arrow indicates minimum Q values corresponding to lowest order Bragg diffraction. On the right side of the figure, deviations of the measured form factor from free-atom form factor, Δ, in terms of a fraction of the valence electron are plotted together with the deviations of the theoretical calculations (dashed line).

In contrast to previous studies with elastic x-ray scattering, which restricts the minimum value of Q to the lowest order Bragg reflection peak ($25.33\ \text{nm}^{-1}$ for lithium, $31.74\ \text{nm}^{-1}$ for beryllium, and $26.87\ \text{nm}^{-1}$ for aluminum, as shown in Fig. 8 with arrows), atomic form factors can be studied directly by phonon intensities without any limitation in the momentum space. Hence, complementary to previous experiments, atomic form-factor measurements are extended to a very low-Q range (down to $1.6\ \text{nm}^{-1}$) using the IXS method. The effect of bonding due to the reconfiguration of the valence electrons for light elements has been directly observed.

ACKNOWLEDGMENTS

The use of the Advanced Photon Source was supported by the Department of Energy, Office of Science, Office of Basic Energy Sciences, under Contract No. DE-ACO2-06CH11357. This work was partially supported by the U.S.

Department of Energy, Division of Material Science, Grant No. DE-FG02-99ER45772. We acknowledge W. Sturhahn for his help with data handling. We would like to thank T. I. Morrison, D. L. Chapman, and C. U. Segre of Illinois Institute of Technology, Chicago, IL, for helpful discussions and advice. We appreciate the help of David Hoogerheide and Xue Wang of Western Michigan University, Kalamazoo, MI, in this experiment.

---

*alatas@aps.anl.gov

†Permanent address: Research Institute for Solid State Physics and Optics, Hungarian Academy of Sciences, Budapest, Hungary.

‡Permanent address: HP-CAT and Carnegie Institution of Washington, Advanced Photon Source, Argonne, IL 60439.

[1] A. J. C. Wilson, *International Tables for Crystallography*, 2nd ed. (Kluwer Academic, Dordrecht, 1995), Vol. C.

[2] P. Coppens, *IUCr Texts on Crystallography 4-X-Ray Charge Densities and Chemical Bonding* (Oxford University Press, Oxford, 1997).

[3] J. Chihara, J. Phys. F: Met. Phys. **17**, 295 (1987).

[4] P. A. Egelstaff, N. H. March, and N. C. McGill, Can. J. Phys. **52**, 1651 (1974).

[5] J. A. Anta and A. A. Louis, Phys. Rev. B **61**, 11400 (2000).

[6] H. Olbrich, H. Ruppersberg, and S. Steeb, Z. Naturforsch. A **38A**, 1328 (1983).

[7] S. Takeda, S. Harada, S. Tamaki, and Y. Waseda, J. Phys. Soc. Jpn. **60**, 2241 (1991).

[8] S. Takeda, M. Inui, S. Tamaki, K. Maruyama, and Y. Waseda, J. Phys. Soc. Jpn. **63**, 1794 (1994).

[9] W. Schülke, H. Nagasawa, S. Mourikis, and P. Lanzki, Phys. Rev. B **33**, 6744 (1986).

[10] G. L. Squires, *Introduction to the Theory of Thermal Neutron Scattering*, 1st ed. (Cambridge University Press, Cambridge, 1978).

[11] E. Burkel, Rep. Prog. Phys. **63**, 171 (2000).

[12] F. Sette, G. Ruocco, M. Krisch, U. Bergmann, C. Masciovecchio, V. Mazzacurati, G. Signorelli, and R. Verbeni, Phys. Rev. Lett. **75**, 850 (1995).

[13] P. J. Brown, Philos. Mag. **26**, 1377 (1972).

[14] N. K. Hansen, J. R. Schneider, and F. K. Larsen, Phys. Rev. B **29**, 917 (1984).

[15] A. G. Fox and R. M. Fisher, Philos. Mag. B **57**, 197 (1988).

[16] B. W. Batterman, D. R. Chipman, and J. J. DeMarco, Phys. Rev. **122**, 68 (1961).

[17] P. Brüesch, *Phonons: Theory and Experiments II*, Solid State Sciences Vol. 65 (Springer, New York, 1986).

[18] T. S. Toellner, Hyperfine Interact. **125**, 3 (2000).

[19] E. Burkel, *Inelastic Scattering of X-Rays with Very High Energy Resolution*, Springer Tracts in Modern Physics Vol. 125, 2nd ed. (Springer, New York, 1991).

[20] H. Sinn, J. Phys.: Condens. Matter **13**, 7525 (2001).

[21] A. Alatas, Ph.D. thesis, Illinois Institute of Technology, 2002.

[22] H. Sinn *et al.*, Nucl. Instrum. Methods Phys. Res. A **467-468**, 1545 (2001).

[23] B. Fåk and B. Dorner, Institute Laue Langevin Technical Report No. 92FA008S, 1992 (unpublished).

[24] M. M. Beg and M. Nielsen, J. Phys. F: Met. Phys. **14**, 4266 (1976).

[25] R. Stedman, Z. Amilius, R. Pauli, and O. Sundin, J. Phys. F: Met. Phys. **6**, 157 (1976).

[26] R. Stedman and G. Nilsson, Phys. Rev. **145**, 492 (1966).

[27] C. Kittel, *Introduction to Solid State Physics*, 7th ed. (Wiley, New York, 1976).

[28] H. Spalt, A. Zounek, B. N. Dev, and G. Materlik, Phys. Rev. Lett. **60**, 1868 (1988).

[29] J. A. Golovchenko, D. R. Kaplan, B. Kincaid, R. Levesque, A. Meixner, M. F. Robbins, and J. Felsteiner, Phys. Rev. Lett. **46**, 1454 (1981).

[30] A. Bosak and M. Krisch, Phys. Rev. B **75**, 092302 (2007).

[31] G. Eckold, UNISOFT, a program package for lattice dynamical calculations, Institut für Kristallographie der RWTH Aachen and Institut für Festkörperforschung der KFA Jülich, 1992.

[32] C. B. Walker, Phys. Rev. **103**, 547 (1956).